Bioactive Materials 5 (2020) 564–568

Contents lists available at ScienceDirect

Bioactive Materials

journal homepage: http://www.keaipublishing.com/biomat

Microstructure, mechanical property and corrosion behavior of porous Ti–Ta–Nb–Zr

B.Q. Li[a,*], R.Z. Xie[a], X. Lu[b]

[a] Mechanics Institute, Jinzhong University, Jinzhong, 030619, China
[b] Liaoning Key Materials Laboratory for Railway, School of Materials Science and Engineering, Dalian Jiaotong University, Dalian, 116028, China

ARTICLE INFO

Keywords:
Porous Ti–Nb–Ta–Zr alloy
Macro-pore structure
Compressive property
Electrochemistry behavior

ABSTRACT

In this paper, biomedical porous Ti–Nb–Ta–Zr with 40% porosity and 166 ± 21 μm macro-pore size was successfully fabricated by space holder method. The microstructure, Vickers hardness, compressive and electrochemistry behavior were studied. It results that a few second phases exist in β matrix of the porous Ti–Nb–Ta–Zr. Its Young's modulus is 0.8 GPa, close to 0.01–3 GPa for trabecular bone. The total recovery strain ratio and pseudoelastic strain ratio are 8.8% and 2.7%, respectively. It fails mainly by brittle cleavage with the fan-shaped and smooth cleaved facets. Although, local ductile fracture by a few dimples and a small amount of transcrystalline fracture with the cleavage of similarly oriented laths in a colony are observed on the fracture surface. The impedance spectrum of porous Ti–Nb–Ta–Zr has the characteristics of half capacitive arc resistance, showing good corrosion resistance in SBF solution.

1. Introduction

Biomaterials that can be implanted into the human body to treat bone disorders, replace bone tissue and restore normal physiological functions of bones should have basic requirements for biomaterials, such as biomechanical compatibility and biomechemistry compatibility. Traditional metal biomaterials involving 316L stainless steel [1], Co–Cr alloy [2], Ti6Al4V [3] and Ti–Ni alloy [4] may lead to allergic problem because of released elements. In comparison, titanium and its alloy without toxic elements have been widely used in biomedical applicant due to excellent biocompatibility. However, the young's modulus of pure titanium (110 GPa) shows higher than that of bone (10–30 GPa for cortical bone; 0.1–2 for cancellous bone), thus causing stress shielding effect [5–9].

In order to prevent stress shielding in postoperative patients, young's modulus of implant should be as low as that of the human bone. Compared to other β-stabilizers, certain Nb and Ta have been found to be more effective in reducing the elastic modulus of β titanium alloys [10–14]. So, Ti–Nb–Ta–Zr alloy has been a new type of titanium alloy developed for biomaterials due to low modulus and improved strength [10–12]. In general, the materials with higher young's modulus show lower resilience, which is more favorable for surgical operations [13,14]. The aim of this paper is to control modulus and pseudoelasticity comprehensively by means of adding pore structure. These pores can reduce modulus but increase bone conductivity. It is published that ideal pore size and porosity are 50–500 μm and 30–90%, respectively [15]. The preparation methods of porous titanium alloys include metallurgical method, casting method, rapid prototyping method, etc [4,7,8,15]. Comparatively, space holder method is relatively mature and easy to operate. The mixing and compaction processes allow customization of material composition, mechanical properties and shapes.

Therefore, in this paper, porous Ti–Nb–Ta–Zr (TNTZ) alloy was produced by space holder method. The mechanical properties and electrochemistry behavior have been investigated based on phase, pores structure and their distribution.

2. Materials and methods

Porous Ti–35Nb–5Ta–7Zr alloy (wt.% hereafter) was prepared by powder metallurgical method using 50 vol% PMMA (polymethyl methacrylate) with the size of 100–154 μm as the space holders. Based on Ref. [16,17], the mixtures were compacted and heat-treated at 250–450 °C for 5 h to remove the space holders, and then sintered at 1200 °C for 2 h in a vacuum diffusion melting furnace. For comparative purpose, similar measurements have been carried on the solid Ti–35Nb–5Ta–7Zr prepared by the same processing but without space holders in green body of mixed powders.

Vickers hardness (HV) measurements were carried out on the pore walls of polished surface of the samples via micro-hardness testing

Peer review under responsibility of KeAi Communications Co., Ltd.
* Corresponding author.
E-mail address: lbq@jzxy.edu.cn (B.Q. Li).

https://doi.org/10.1016/j.bioactmat.2020.04.014
Received 7 November 2019; Received in revised form 8 April 2020; Accepted 19 April 2020

Fig. 1. Equivalent circuit.

machine (FM700). A load of 100 g was applied for 15 s (dwell time). Eleven different measurements were performed for each sample group and the maximum and minimum values were not taken into calculation. The homogeneity index *HI* ($HI = \frac{S}{Hm}$) of porous samples were calculated directly by measuring the microhardness of porous titanium alloy, based on the Ref. [18], reflecting the pore distribution of porous sample. Where *S* is standard deviation of hardness, *Hm* is mean hardness.

The compressive properties of porous samples were studied using SANS-CMT 5205 at a constant strain rate of 0.001/s. A compression cage with hard-metal platens was used to assure parallelism, with an extensometer attached to the platens to determine the elastic modulus. The 0.2%-offset method was used to determine the yield strength of porous samples. At least three measurements were carried out under the same conditions, and the mean values were calculated. The total recovery strain ratio ($\varepsilon_e + \varepsilon_s/\boldsymbol{\varepsilon_{total}}$) and pseudoelastic strain ratio ($\varepsilon_s/\varepsilon_{total}$) were then evaluated based on compressive testing data from the stress-strain curves as illustrated in Ref. [16,19].

The electrochemical analysis system of chi660e was used for corrosion performance test. The scanning rate was 0.01 V/s, and the electrolyte was SBF solution [20]. Since the sample test shows that the impedance spectrum presents the characteristics of a time constant [21,22], the equivalent circuit shown in Fig. 1 is used to fit the impedance spectrum. Among them, *R1* is the solution resistance, *R2* is the charge transfer resistance, *CPE* is the interface double electric layer capacitance, including *CPE-T* (interface double electric layer capacitance) and *CPE-P* (representing the degree of deviation of the interface capacitance from the ideal capacitance). The closer *CPE-P* is to 1, the closer interface capacitance is to ideal capacitance. The higher *R2* is, the better the corrosion resistance of the material is.

3. Results and discussion

Fig. 2 demonstrates the SEM images of powder and porous TNTZ with 50% space holder of 100–154 μm. The mean size of angular mixed

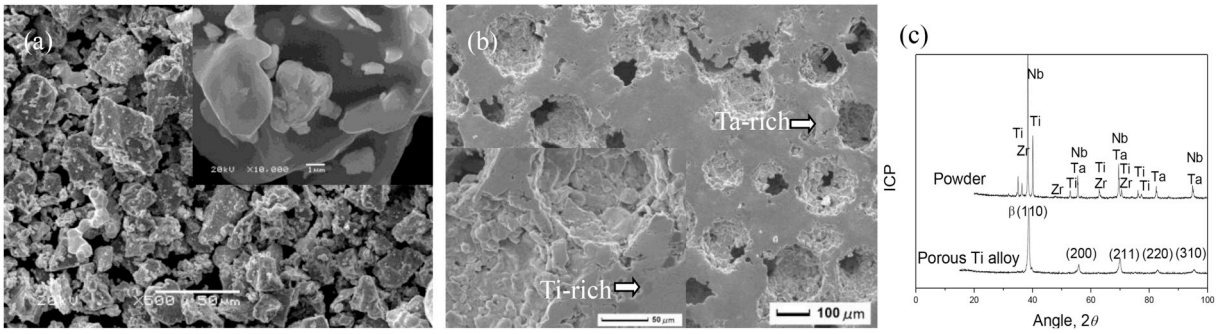

Fig. 2. Microstructure of Powder (a) and porous TNTZ alloy (b) and XRD diffraction (c).

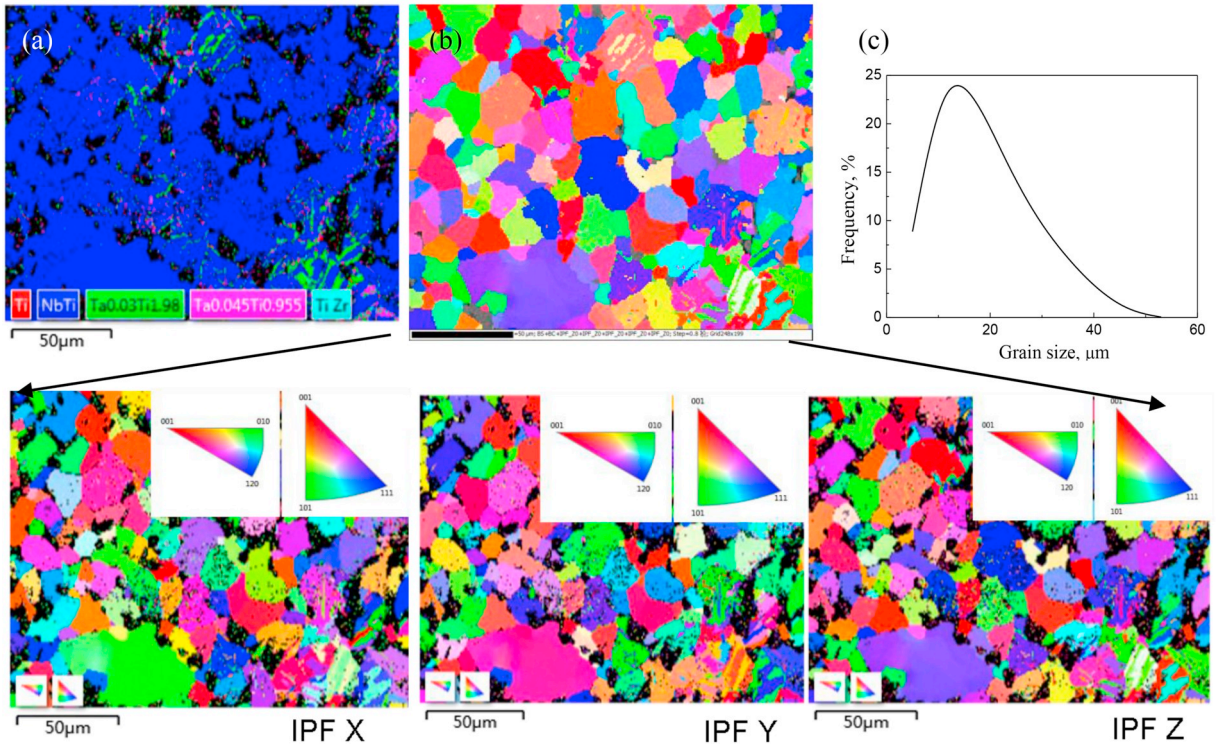

Fig. 3. EBSD results of TNTZ alloy: (a) Phase distribution; (b) Grain distribution; (c) Grain size distribution.

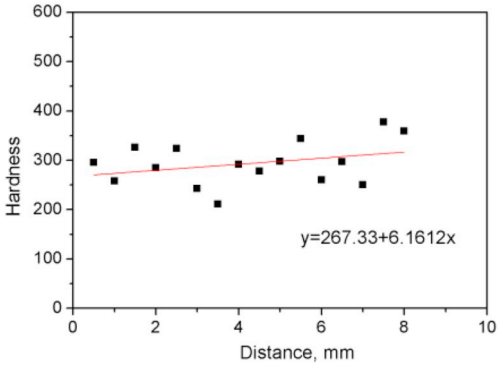

Fig. 4. Micro-hardness distribution of porous TNTZ.

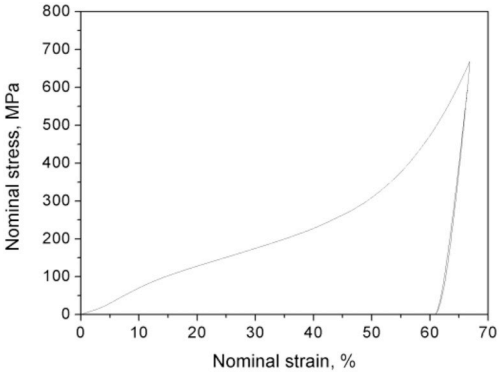

Fig. 5. Stress-strain curve of porous TNTZ alloy.

powders (see Fig. 2 a) used here is 28 ± 10.10 μm. Porous Ti–Nb–-Ta–Zr has a three-dimensional connected open pore structure (40%), and its pores can be divided into two types: macro-pores (166 ± 21 μm, suitable for the growth of bone cells) and micro-pores (12 μm ± 2.15 μm) distributed on the wall of macro-pore. Combined the EBSD results of solid TNTZ without space holder at the same sintering condition in Fig. 3, a few second phases (such as Ta-rich and Ti-rich phases in Fig. 2 b) distribute irregularly in grain β TiNb matrix and may be caused by microstructure inhomogeneity of powder metallurgy, which is consistent with the EDS result in Ref. [17]. The mean grain size is 21.35 ± 7.4 μm.

It refers to the idea of using the homogeneity index *HI* [16] to reflect the distribution of pores (weakening hardness value) and second phases. Fig. 4 represents the micro-hardness distribution of porous TNTZ. The hardness range is 157–440, and the distribution of micro-hardness is y = 267.33 + 6.1612 x by linear fitting. The homogeneity index *HI* is 0.78. It can be seen the hardness distribution in this paper is controlled by the coordination of micropore and second phase distribution.

Stress-strain curve obtained by cyclic loading-unloading compressive tests for the porous TNTZ in Fig. 5 reveals significant recovery of elastic strain and pseudoelastic character, similar to solid Ti–Nb–Ta–Zr alloy obtained by AM and PM [19]. In this cycle, the stress was applied up to 669 MPa when strain reached at 66.9%, and then the stress was removed. The total recovery strain ratio and pseudoelastic strain ratio of porous TNTZ are 8.8% and 2.7%, respectively, far below than 69.4% and 12.3% for bulk samples prepared by the same processing but without space holders in green body of mixed powders. It is mainly related to the movement of twin-boundaries and slip and the deformation twinning and strain-induced martensitic [16]. The Young's modulus of porous TNTZ is 0.8 GPa, close to 0.01–3 GPa for trabecular bone [23].

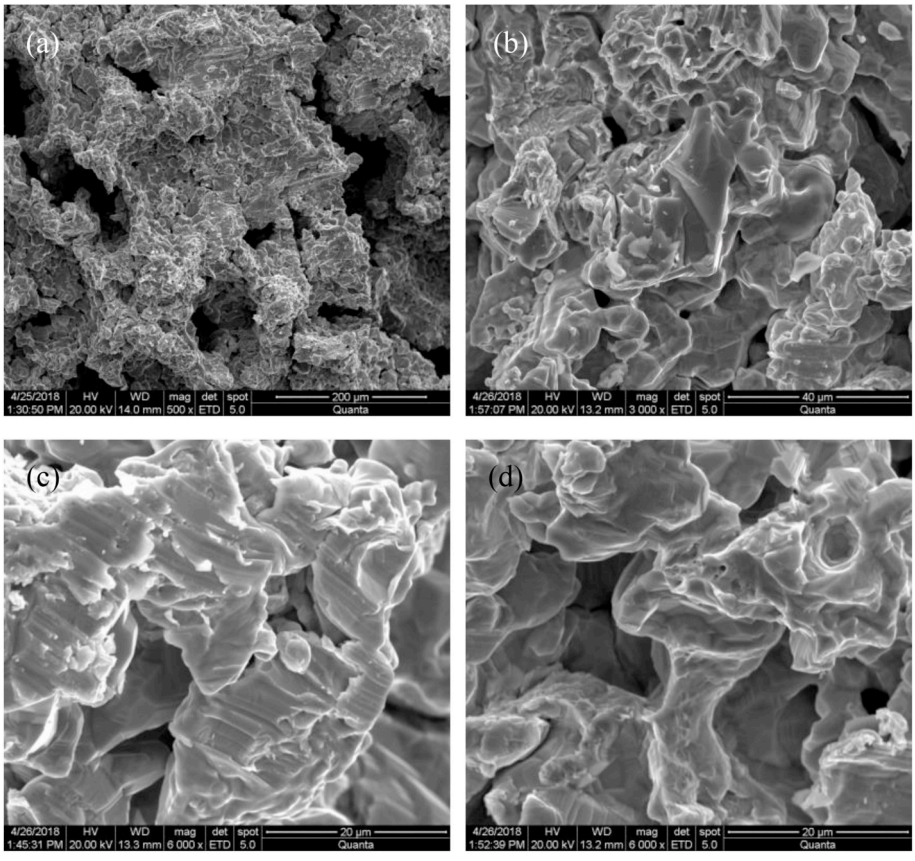

Fig. 6. SEM fractography of the porous TNTZ under compression showing: (a) macro-cracks, (b) cleavage facets, (c) transcrystalline fracture and (d) micro-voids.

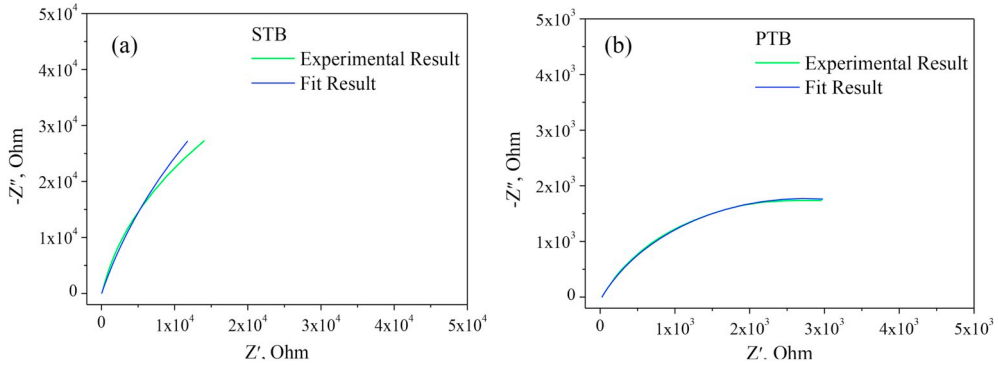

Fig. 7. The Nyquist diagram of solid (a) and porous TNTZ (b).

Table 1
Fitting parameters of Nyquist results.

Samples	R_1(Ohm·cm^2)	R_2(Ohm·cm^2)	*CPE*	
			CPE-T (S·s^{-n}·cm^{-2})	CPE-P
STB	20.85	1.878E5	1.239E-4	0.838
PTB	23.93	5.426E3	4.638E-4	0.736

The compressive fractographies for the porous TNTZ in Fig. 6 illustrate the macro-pore-initiated cracks and the second cracks distributed along the micro-pores. The cleavage fracture (Fig. 6 b) and transcrystalline fracture with the cleavage of similarly oriented laths in a colony (Fig. 6 c) can be observed. Local ductile fracture by a few irregular dimples are also found around the tear ridges in Fig. 6 (d), and thus forming the plastic hinge. It is revealed that the mode of failure for porous TNTZ is mainly brittle cleavage with the fan-shaped and smooth cleaved facets. Although, local ductile fracture by a few dimples and a small amount of transcrystalline fracture with the cleavage of similarly oriented laths in a colony are observed on the fracture surface.

Fig. 7 shows the Nyquist diagram and the equivalent circuit fitting results of solid TNTZ (STB) and porous TNTZ (PTB). Obviously, the impedance spectra of the two materials show the characteristics of half capacitive arc resistance. The impedance spectrum radius of the solid alloy is larger, showing higher corrosion resistance. It is consistent with the results of the anodic polarization curve in Ref. [19]. According to the fitting parameters in Table 1, the fitting results of corresponding equivalent circuits are good. The solution resistance *R1* is small, and the values are all around 20 Ohm•cm^{-2}. The charge transfer resistance *R2* of the solid alloy is relatively large, reaching 1.878E5 Ohm•cm^{-2}, with good corrosion resistance, but 35% less than that of the melted alloy (AM). The *CPE-P* value of porous TNTZ is 0.736 and deviates from the ideal capacitance. It may be related to the larger porous surface exposed to corrosion environment because of interconnected macro-pores. Additionally, it is assumed that the mechanisms for porous TNTZ are a consequence of the presence of broader active-passive transition and the unstable passive region in SBF solution, as described in Ref. [16]. Such corrosion attack probably occurs within the channels and on rough macro-pore walls, and thereby these weak regions provide the

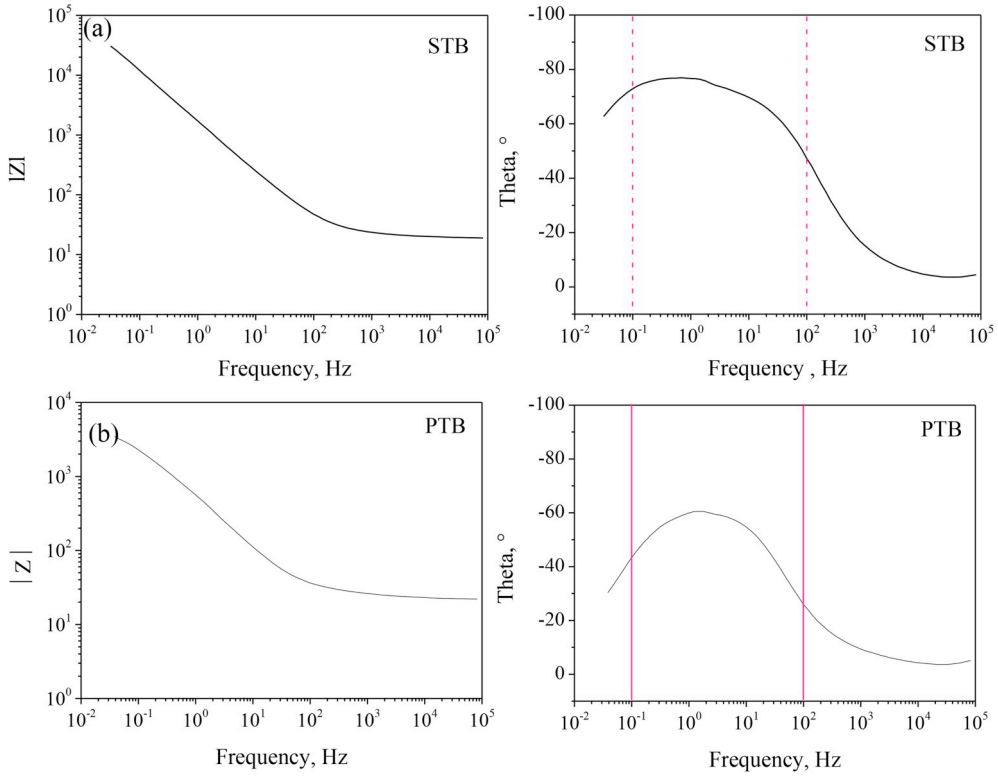

Fig. 8. The Bode diagram of solid (a) and porous (b) TNTZ.

bare active sites that are capable of trapping liquid.

As can be seen form Fig. 8, the Bode mode values of the two alloys are consistent with the impedance spectrum. The phase angle has a peak value between 10^{-1}–10^{2} Hz in a wide frequency domain. Compared with solid alloy, the phase angle peak of porous alloy is obvious, and the peak value decreases, reflecting its low corrosion resistance to some extent. However, compared with other porous materials, the porous TNTZ still shows excellent corrosion resistance [24]. Therefore, it indicates that present porous TNTZ with high mechanical strength and low pseudoelastic strain has potential application for bone implants.

4. Conclusions

1) Porous Ti–Nb–Ta–Zr with 40% porosity and 166 ± 21 μm macropore size for biomedical applications were successfully fabricated by space holder method. A few second phases distribute uniformly in β TiNb matrix, and the mean grain size is 21.35 ± 7.4 μm.
2) The total recovery strain ratio and pseudoelastic strain ratio of porous TNTZ are 8.8% and 2.7%, respectively. The Young's modulus of porous TNTZ is 0.8 GPa, close to 0.01–3 GPa for trabecular bone.
3) Porous TNTZ fails mainly by brittle cleavage with the fan-shaped and smooth cleaved facets. Although, local ductile fracture by a few dimples and a small amount of transcrystalline fracture with the cleavage of similarly oriented laths in a colony are observed on the fracture surface.
4) The impedance spectrum of porous TNTZ shows the characteristics of half capacitive arc resistance, and the phase angle has a peak value between 10^{-1}–10^{2} Hz in a wide frequency domain, showing good corrosion resistance in SBF solution.

Declaration of competing interest

There is no conflict of interest.

Acknowledgements

This work was supported by “1331” Innovation Team of Jinzhong University (jzxycxtd2019008) and research project under Grant No. 201801D221095 from Natural Science Foundation of Shanxi Province (CN).

References

[1] A. Latifi, M. Imani, M.T. Khorasani, M.D. Joupari, Plasma surface oxidation of 316L stainless steel for improving adhesion strength of silicone rubber coating to metal substrate, Appl. Surf. Sci. 320 (2014) 471–481.
[2] B.V. Hooreweder, K. Lietaert, B. Neirinck, N. Lippiatt, M. Wevers, CoCr F75 scaffolds produced by additive manufacturing: influence of chemical etching on powder removal and mechanical performance, J. Mech. Behav. Biomed. Mater. 70 (2017) 60–67.
[3] M. Fazel, H.R. Salimijazi, M. Shamanian, I. Apachitei, A.A. Zadpoor, Influence of hydrothermal treatment on the surface characteristics and electrochemical behavior of Ti-6Al-4V bio-functionalized through plasma electrolytic oxidation, Surf. Coating. Technol. 374 (2019) 222–231.
[4] Y. Kim, Mechanical properties of highly porous Ti49.5Ni50.5 biomaterials, Intermetallics 62 (2015) 56–59.
[5] P. Tengvall, I. Lundström, Physico-chemical considerations of titanium as a biomaterial, Clin. Mater. 9 (1992) 115–134.
[6] M. Long, H.J. Rack, Titanium alloys in total joint replacement–a materials science perspective, Biomaterials 19 (1998) 1621–1639.
[7] J. Liu, J. Ruan, L. Chang, H. Yang, W. Ruan, Porous Nb-Ti-Ta alloy scaffolds for bone tissue engineering: fabrication, mechanical properties and in vitro/vivo biocompatibility, Mater. Sci. Eng. C 78 (2017) 503–512.
[8] Y. Li, J. Xiong, P.D. Hodgson, C. Wen, Effects of structural property and surface modification of Ti6Ta4Sn scaffolds on the response of SaOS2 cells for bone tissue engineering, J. Alloys Compd. 494 (2010) 323–329.
[9] X. Zhao, M. Niinomi, M. Nakai, G. Miyamoto, T. Furuhara, Microstructures and mechanical properties of metastable Ti–30Zr–(Cr, Mo) alloys with changeable Young's modulus for spinal fixation applications, Acta Biomater. 7 (2011) 3230–3236.
[10] R. Karre, M.K. Niranjan, S.R. Dey, First principles theoretical investigations of low Young's modulus beta Ti-Nb and Ti-Nb-Zr alloys compositions for biomedical applications, Mater. Sci. Eng. C 50 (2015) 52–58.
[11] S. Acharya, A.G. Panicker, D.V. Laxmi, S. Suwas, K. Chatterjee, Study of the influence of Zr on the mechanical properties and functional response of Ti-Nb-Ta-Zr-O alloy for orthopedic applications, Mater. Des. 164 (2019) 107555.
[12] S. Ozan, J. Lin, Y. Li, C. Wen, New Ti-Ta-Zr-Nb alloys with ultrahigh strength for potential orthopedic implant applications, J. Mech. Behav. Biomed. Mater. 75 (2017) 119–127.
[13] M. Niinomi, T. Akahori, M. Nakai, H. Tsutsumi, Effects of thermomechanical treatments on pseudoelastic strain characteristics of Ti-29Nb-13Ta-4.6 Zr for biomedical applications, Mater. Trans. 50 (2009) 1704–1712.
[14] D. Kent, G. Wang, Z. Yu, M.S. Dargusch, Pseudoelastic behaviour of a β Ti–25Nb–3Zr–3Mo–2Sn alloy, Mater. Sci. Eng., A 527 (2010) 2246–2252.
[15] M. Takemoto, S. Fujibayashi, M. Neo, J. Suzuki, T. Kokubo, T. Nakamura, Mechanical properties and osteoconductivity of porous bioactive titanium, Biomaterials 26 (2005) 6014–6023.
[16] B.Q. Li, C.L. Li, X. Lu, Compressive property and electrochemistry behavior of porous Ti-Nb-Ta-Zr for biomedical applications, Key Eng. Mater. 803 (2019) 178–181.
[17] B.Q. Li, X. Lu, A biomedical Ti-35Nb-5Ta-7Zr alloy fabricated by powder metallurgy, J. Mater. Eng. Perform. 28 (2019) 5616–5624.
[18] C.F. Li, Z.G. Zhu, T. Liu, Microhardness of pore walls in porous titanium prepared with novel powder metallurgy, Powder Metall. 48 (2005) 237–240.
[19] B.Q. Li, C.L. Li, Z.X. Wang, X. Lu, Preparation of Ti-Nb-Ta-Zr alloys for load-bearing biomedical applications, Rare Met. 38 (2019) 571–576.
[20] T. Kokubo, H. Takadama, How useful is SBF in predicting in vivo bone bioactivity? Biomater 27 (2006) 2907–2915.
[21] E. Barsoukov, J.R. Macdonald, Impedance Spectroscopy Theory, Experiment, and Applications, John Wiley & Sons, Hoboken, New Jersey, 2005.
[22] C.N. Cao, J.Q. Zhang, An Introduction to Electrochemical Impedance Spectroscopy, Science Press, Beijing, 2002.
[23] S.A. Goldstein, The mechanical properties of trabecular bone: dependence on anatomic location and function, J. Biomech. 20 (1987) 1055–1061.
[24] X.P. Li, Corrosion Behavior of TiN and TiN/Ti Coated on 303 Stainless Steel, Taiyuan University of Technology, Taiyuan, 2016.